Asian Journal of Chemistry; Vol. 37, No. 1 (2025), 135-144

ASIAN JOURNAL OF CHEMISTRY

https://doi.org/10.14233/ajchem.2025.32918

Structure, Morphology, DC-Electrical and Dielectric Characteristics of Chromium(III) Substituted Co-Li Ferrite Nanoparticles

ASHA A. NAWPUTE[1,*], S.V. RAJMANE[2], SUDARSHAN D. TAPSALE[3] and K.M. JADHAV[1,4]

[1]Department of Physics, Dr. Babasaheb Ambedkar Marathwada University, Chhatrapati Sambhajinagar (Aurangabad)-431004, India
[2]Department of Physics, Jawahar Arts, Science & Commerce College, Andur-413603, India
[3]Department of Education and Extension, Chemistry Science, Savitribai Phule Pune University, Pune-411007, India
[4]School of Basic and Applied Sciences, MGM University, Chhatrapati Sambhajinagar (Aurangabad)-431003, India

*Corresponding author: E-mail: nawputea@gmail.com

Received: 19 October 2024; *Accepted*: 7 December 2024; *Published online*: 31 December 2024; AJC-21860

In this study, a detailed analysis of the lattice structure, micro-structural features, DC-electrical properties and dielectric characteristics of Cr^{3+}-substituted cobalt-lithium-based ferrite oxide nanoparticles (CoLiFCr NPs) synthesized using a sol-gel method enhanced by synergistic sol-gel auto-combustion is presented. Citric acid monohydrate ($C_6H_8O_7{\cdot}H_2O$) was utilized as a chelating agent, maintaining a metal nitrate to citrate ratio of 1:3. Substituting Cr^{3+} in Co-Li ferrite significantly alters its crystal structure, morphological, DC-electrical and dielectric characteristics. The X-ray diffraction (XRD) analysis confirmed the crystalline formation of $Co_{0.8}Li_{0.4}Fe_{2-x}Cr_xO_4$ nanoparticles (where x = 0.0, 0.2, 0.4 and 0.6); exhibiting the single-phase cubic structure characterized by a spinel configuration, falling under the space group Fd-3mO_h^7. The lattice constant a for CoLiFCr NPs (x = 0) was measured at 8.338 ± 0.002 Å, which decreased to 8.291 ± 0.002 Å upon Cr substitution (x = 0.6), as confirmed by Cohen's analytical graphs. The crystallite size (D), determined using the Debye-Scherrer's formula, ranged from around 18.9 to 29.74 nm. Peak broadening in CoLiFCr NPs was further examined through Williamson-Hall and size strain analyses. The FTIR spectra of CoLiFCr nanoparticles revealed the presence of metal-oxygen (M-O) bonds typical of spinel structures, featuring significant peaks at 443 cm^{-1} and 537 cm^{-1}. High-resolution transmission electron microscopy (HR-TEM) images showed the single-crystal CoLiFCr NPs with nearly spherical morphologies. The study of optical properties was conducted using UV-visible spectroscopy. The nanoparticles with x = 0.2 displayed high ε' values at 50 Hz, indicating strong polarization capabilities, while those with x = 0.6 exhibited a decrease possibly linked to structural changes affecting polarization. The DC resistivity of CoLiFCr nanoparticles was investigated to understand their electrical behaviour highlighting the influence of substitution of Cr^{3+} on conductivity.

Keywords: Chromium(III), Co-Li Nanoferrites, Sol-gel auto-combustion, W-H plot, Cohen's graphs, Dielectric property.

INTRODUCTION

In recent times, there has been a growing interest in investigating spinel ferrite nanoparticles because of their remarkable structural, dielectric and magnetic characteristics. These nanoparticles are part of the spinel ferrite group, defined by the general formula (AB_2O_4), with A and B denoting divalent and trivalent metal cations, respectively [1]. Cobalt-lithium ferrite nanoparticles (Co-Li ferrite NPs) are of particular interest because of their potential applications in high-frequency devices, magnetic storage, catalysis and biomedical fields. By incorporating different dopants into the ferrite matrix, we can further customize these properties, resulting in improved performance for specific applications. The inclusion of lithium not only enhances the electrical properties but also has a significant impact on the magnetic characteristics of the nanoparticles. This remarkable combination of features is especially advantageous for applications such as magnetic resonance imaging (MRI) [2], where both high magnetic saturation and low dielectric losses are desirable. In the case of Co-Li ferrite NPs, cobalt (Co^{2+}) and lithium (Li^+) ions occupy the tetrahedral (A) and octahedral [B] sites of the spinel structure, resulting in a versatile material with a wide range of applications, including high-density magnetic storage, biomedical imaging and drug delivery. The ability to substitute different cations, such as chromium (Cr^{3+}), into the ferrite structure allows for precise adjustment of the material's

properties to meet specific application requirements. Chromium doped cobalt-lithium ferrite nanoparticles (CoLiFNPs) are gaining prominence as crucial materials in a wide range of cutting edge applications, driven by their improved magnetic, dielectric and structural characteristics [3]. One exciting field of development is high-density magnetic storage devices, where the remarkable magnetic saturation (ranging from 60-80 emu/g) and consistent performance across different temperatures can greatly improve both storage capacity and data access speeds. Moreover, in biomedicine, these nanoparticles show significant promise for targeted drug delivery and magnetic resonance imaging (MRI). Their compatibility with biological systems, along with the capability to alter their surfaces, enables accurate targeting of cancer cells, reducing side effects and enhancing the effectiveness of treatments [4]. Significantly, their super-paramagnetic behaviour at room temperature (with a blocking temperature below 300 K) ensures minimal residual magnetism, which is crucial for MRI contrast agents [5].

Researchers also actively explored Cr-doped CoLiFNPs for their potential in wastewater treatment and remediation. Their high surface area and reactivity make them effective at adsorbing and breaking down pollutants [6]. In the energy sector, they are being incorporated into cutting-edge battery technologies and supercapacitors, taking advantage of their distinctive electrochemical characteristics, including a high specific capacitance of up to 400 F/g and outstanding cyclic stability, maintaining over 90% of their capacitance even after 1000 cycles [7]. The unique electrical characteristics, with a dielectric constant (ε′) ranging from 50 to 200, along with their magnetic features, enable the development of advanced sensors used in industrial automation [7], healthcare and environmental monitoring [8]. Thus, keeping in mind about these facts, this study aims to synthesize and comprehensively characterize chromium substituted cobalt-lithium ferrite nanoparticles (CoLiFNPs) using the sol-gel method. The sol-gel method combined with auto-combustion is an effective way to obtain high-purity nanoparticles.

EXPERIMENTAL

The synthesis of Cr-substituted cobalt-lithium ferrite nanoparticles (CoLiFCr NPs) utilized the analytical-graded chemicals. The raw materials include analytical grade cobalt nitrate [$Co(NO_3)_2{\cdot}6H_2O$] and ferric nitrate [$Fe(NO_3)_3{\cdot}9H_2O$]. Lithium nitrate was used to introduce lithium ions (Li^+), which enhance the magnetic properties and structural stability of ferrite. Chromium nitrate [$Cr(NO_3)_3{\cdot}9H_2O$] was added for the chromium ions (Cr^{3+}) that substitute the iron ions in the octahedral [B]-site, influencing the magnetic and electrical properties of the material. Citric acid [$C_6H_8O_7{\cdot}H_2O$] acts as a chelating agent and binds the metal ions togather to ensure a uniform mixture and also controls the particle size during synthesis. The pH was adjusted using ammonia solution, which facilitates the precipitation of metal hydroxides. Acetone was employed in the washing process to remove impurities and residual organics, while double distilled water was used to maintain the solution purity and prevent contamination. The accurately measured and combined reagents in stoichiometric ratios were presumed to yield the intended chemical composition and structural characteristics, reducing impurities and ensuring optimal performance.

Synthesis of CoLiFCr NPs: In the sol-gel synthesis of $Co_{0.8}Li_{0.4}Fe_{2-x}Cr_xO_4$ NPs (where x = 0.0, 0.2, 0.4 and 0.6), the process began with precise measurement of metal precursors. These precursors were hydrolyzed in an aqueous solution with vigorous stirring and heating at 80 ºC for 3 h to maintain a neutral pH of 7 by gradually adding ammonia solution to the nitrate solution. As the poly-condensation process continued, water was slowly removed while the solution was stirred on a magnetic hot plate. The transition from the sol phase to the viscous gel phase was achieved gradually, with citric acid playing a key role in complexing various metal ions to prevent selective precipitation and ensure a uniform composition. As the mixture of nitrate and citrate was heated further, its temperature rose to 120 ºC, triggered an auto-catalytic combustion reaction. This reaction produces high temperatures, which help reduce metal ions to their oxides and promote nucleation and crystallization in the gel. The dry-gel then underwent an exothermic reaction known as auto-combustion that results in the formation of agglomerated crystalline structures. The CoLiFCr nanoparticles were dried and annealed at 650 ºC for 4 h to monitor crystallization and phase transformation, ensuring the desired structural and magnetic properties were achieved [9].

RESULTS AND DISCUSSION

Thermogravimetric analysis: The percentage weight loss in relation to temperature (T) is depicted in Fig. 1a-d for $Co_{0.8}Li_{0.4}Fe_{2-x}Cr_xO_4$ NPs (x = 0.0, 0.2, 0.4, 0.6). The thermogravimetric analysis (TGA) reveals a weight loss occurring around 250 ºC, which likely indicates the elimination of impurities and moisture. A key broad peak between 600-800 ºC signifies the complete crystallization of $Co_{0.8}Li_{0.4}Fe_{2-x}Cr_xO_4$ NPs. After reaching this temperature range, there is no further significant weight loss, implying that the material remains stable without any decomposition. The differential thermal analysis (DTA) curve points to approximately 600 ºC as the ideal temperature for achieving complete ignition and stable phase formation. The TGA and DTA results for $Co_{0.8}Li_{0.4}Fe_{2-x}Cr_xO_4$ NPs (x = 0.0) shed light on the thermal behaviour and stability of the material. The TGA curve indicates an initial weight loss up to around 250 ºC, attributed to the removal of moisture and impurities, suggesting the presence of adsorbed water or other volatile components. A significant broad peak is observed between 600-800 ºC, marking the crystallization of $Co_{0.8}Li_{0.4}Fe_{2-x}Cr_xO_4$ NPs, which indicates substantial structural transformations leading to the crystalline phase. Beyond 800 ºC, the absence of significant weight loss confirms the thermal stability of material, indicating that it has fully crystallized with no further decomposition or reactions taking place. The DTA curve reveals an endothermic peak reaching about 250 ºC, which corresponds with the initial weight loss in the TGA curve. This suggests that heat is being absorbed as impurities and moisture are removed. Additionally, there is an exothermic peak near 600 ºC in the DTA curve, which is linked to the crystallization process, signi-

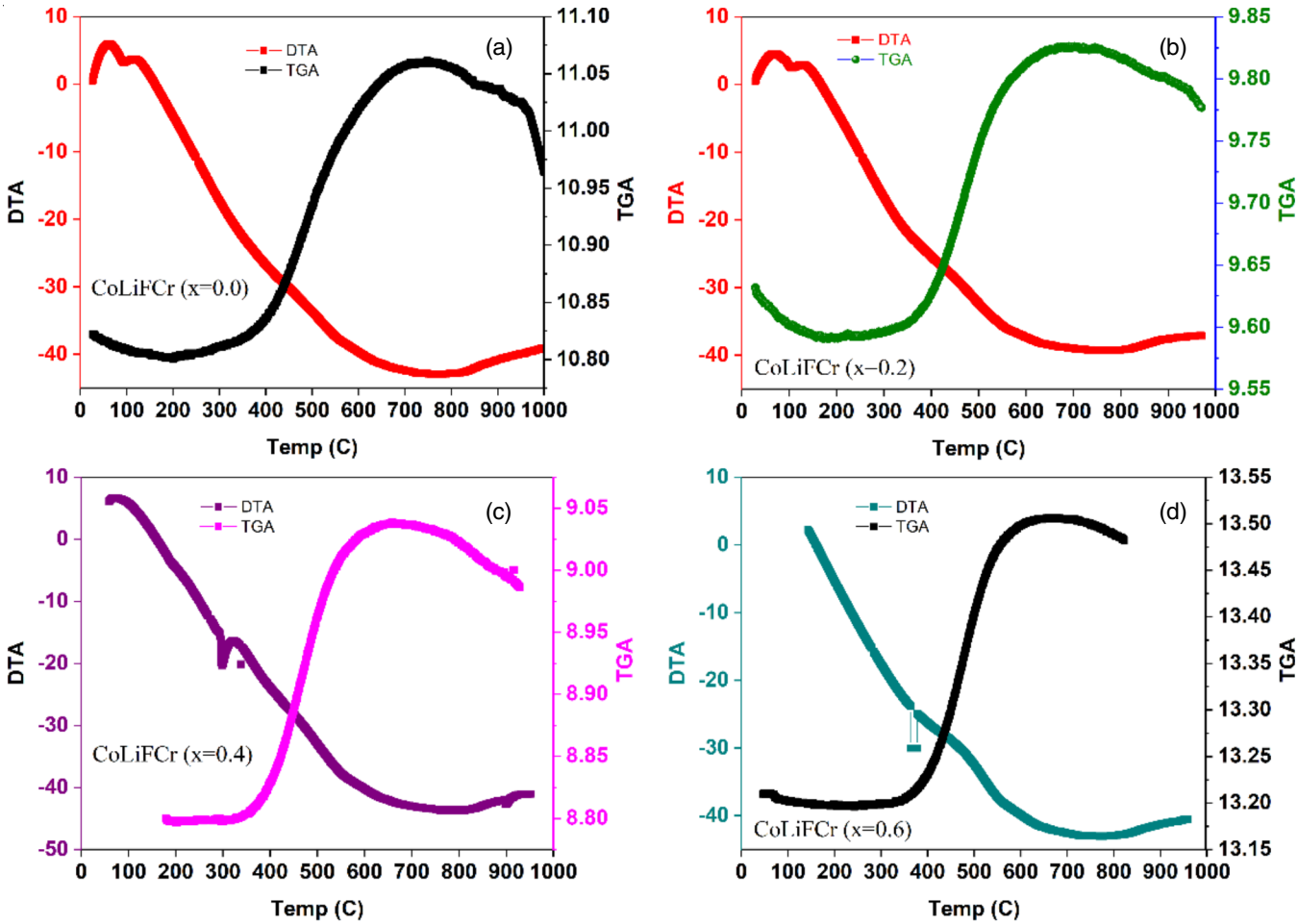

Fig. 1. (a-d) TGA-DTA plots for $Co_{0.8}Li_{0.4}Fe_{2-x}Cr_xO_4$ FNPs (where x = 0.0, 0.2, 0.4 and 0.6)

fying energy release as the sample forms a stable crystalline structure. After 800 ºC, the DTA curve levels off, indicating that no further thermal changes occur, thus confirming the stability of the crystalline phase as supported by the TGA results.

XRD studies: Employing Cu$K\alpha$ radiation (λ = 1.5409 Å) at room temperature, with a normalization set at 40 mA current and 40 kV voltage, the X-ray diffractometer (X'PertPRO MPD PANAlytical) was utilized to investigate the diffraction profiles of CoLiFCr nanoparticles (x = 0.0, 0.2, 0.4 and 0.6). To evaluate the phase purity and structural characteristics of CoLiFCr NPs, the XRD pattern was captured across the 2θ range of 20º to 80º at a scanning rate 2º/min. Fig. 2 displays the presence of reflections such as (220), (311), (222), (400), (422), (511), (440) and (533), signifying the crystalline phases present, which closely aligned with JCPDS card No. 74-2081 and 44-1485, confirming the FCC-type single-phase cubic spinel structure of CoLiFCr NPs in space group Fd-3mO_h^7 [10-12]. The steady nature of the XRD pattern, which shows no phase shifts, along with the arrangement of atoms in the crystal lattice, suggests that there may be a shift from order to disorder in the cation sub-networks that drive structural changes.

Lattice constant: In CoLiFCr NPs, where x ranges from 0.0 to 0.6, the lattice constant generally decreases as the Cr content increases. This phenomenon is primarily due to the smaller ionic radius of Cr^{3+} in comparison to Fe^{3+}, resulting in

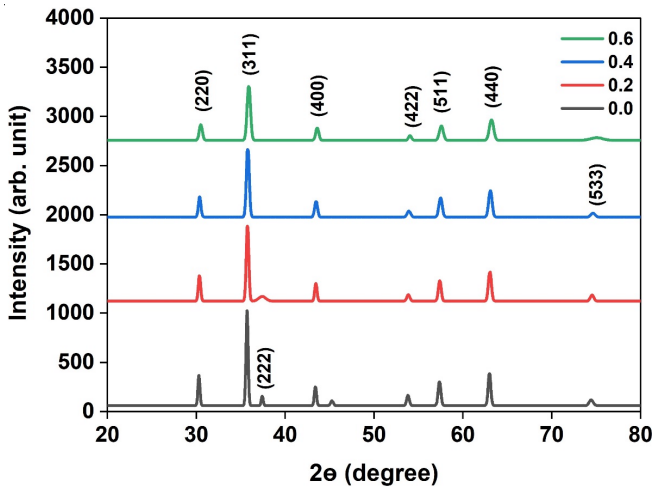

Fig. 2. X-ray diffraction pattern of CoLiFCr NPs (where x = 0.0, 0.2, 0.4 and 0.6)

a contraction of the unit cell. For instance, the lattice constant 'a' for $Co_{0.8}Li_{0.4}Fe_2O_4$ (x = 0) is typically measured at around 8.338 ± 0.002 Å, while for $Co_{0.8}Li_{0.4}Fe_{1.4}Cr_{0.6}O_4$ (x = 0.6), the lattice constant decreases to approximately 8.291 ± 0.002 Å (Table-1). This reduction in lattice constant is confirmed through XRD analysis as shown in Fig. 3. The accurate determination of the lattice constant involves the application of

TABLE-1
BRAGG'S ANGLE (2θ), LATTICE CONSTANT (a) Å, THE CRYSTALLITE SIZE (D) FOR THE CoLiFCr NPs (WHERE x = 0.0, 0.2, 0.4 AND 0.6)

	(a) Å		D (Sherrer)	D (W-H)	Crystallinity	Dislocation density	Lattice strain	Macrostrain
x	a	dx	(nm)	(nm)	(%)	$\delta \times 10^3$ (nm^{-2})	$\varepsilon \times 10^{-3}$	10^{-4}
0.0	8.338	5.1798	29.74	64.8	40.36	1.129	0.394	18.1
0.2	8.328	5.1776	25.03	32.4	42.90	1.595	0.469	15.2
0.4	8.306	5.1692	22.32	32.1	41.85	2.006	0.527	13.3
0.6	8.291	4.8072	18.90	25.1	50.39	2.799	0.625	10.4
			24.00					

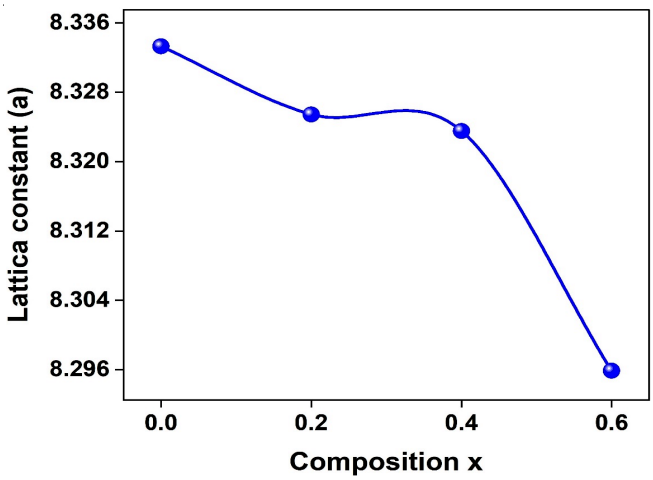

Fig. 3. Lattice constant of CoLiFCr NPs (where x = 0.0, 0.2, 0.4 and 0.6)

Bragg's law to the indexed peaks obtained from the XRD pattern, with a specific formula utilized for calculating the lattice constant in cubic structures [13,14] as eqn. 1;

$$a = \sqrt{(h^2 + k^2 + l^2)} \cdot \frac{\lambda}{\sin\theta} \quad (1)$$

where h, k and l are the Miller indices of the crystal planes; λ is the wavelength of X-ray source and θ is the diffraction angle. The incorporation of Cr^{3+} ions in Co-Li ferrite nanoparticles (x = 0.2, 0.4 and 0.6) leads to a decrease in the lattice constant, trending towards approximately 8.291 ± 0.002 Å. This reduction is primarily due to the smaller ionic radius of Cr^{3+} (0.615 Å) compared to that of Fe^{3+} (0.645 Å). The decrease in the lattice constant can also be attributed to the conversion of ferric ions (Fe^{2+}), which have a higher ionic radius (0.76 Å for high-spin d^6 ions), to ferrous ions (Fe^{3+}) with a lower ionic radius (0.64 Å). The dual effect of Cr^{3+} substitution and the conversion of Fe ions results in the observed contraction of the crystal lattice.

Crystallite size (D_{311}): The crystallite size (D) of the citric acid assisted sol-gel produced CoLiFCr NPs was estimated using the Debye-Scherrer's formula, which is particularly effective for well-defined and distinct peaks, such as (311) peak. The formula is given by Basak *et al*. [15] as eqn. 2:

$$D_{311} = \frac{k\lambda}{\beta\cos\theta} \quad (2)$$

In eqn. 2, D represents the volume-averaged crystallite size; β denotes the full width at half maximum (FWHM) of (311) peak; λ stands for the X-ray wavelength; θ indicates the diffraction angle and k is a shape factor, usually taken as 0.89.

If we assume the sample is mono-domain and free of strain, the crystallite size D_{311} for CoLiFNPs sample with x = 0.0 was found to be around 29.74 nm. This size gradually decreased to about 18.90 nm with increasing Cr^{3+} co-substitution (Table-1). The x = 0 sample exhibited interesting behaviour in terms of crystallite size, which warrants further discussion [16]. There is a general trend of decreasing lattice constant (a) with a decrease in crystallite size D_{311}. This behaviour can be attributed to the lattice striving to reach a state of minimum energy as the crystallite size decreases. This phenomenon aligns with observations reported in several studies. The reduction in crystallite size with Cr^{3+} substitution likely results from the strain and defects introduced by the smaller Cr^{3+} ions (0.615 Å) replacing the larger Fe^{3+} ions (0.645 Å), causing the lattice to contract and form smaller, more stable crystallites [17].

X-ray density values (d_x): The X-ray density (d_x) is a theoretical density calculation based on the crystal structure and composition of the material. For CoLiFCr NPs, the X-ray density was measured in the range of 5.1798 g/cm^3 to 4.8072 g/cm^3. This variation is influenced by the specific composition and crystallographic parameters of the nanoparticles. The X-ray density is determined using eqn. 3 [18]:

$$d_x = \frac{Z.M}{N_A.V} \quad (3)$$

The quantity Z represents the number of formula units contained within a single unit cell. The symbol M denotes the molar mass of each formula unit; N_A represents Avogadro's number (6.022×10^{23} mol^{-1}); V signifies the volume of unit cell substitution of Cr ions, which can affect the molar mass and unit cell volume, thereby influencing the X-ray density [19] (Table-1). The Archimedes method is utilized to determine the bulk density (d_B) of sintered CoLiFCr NPs, which gives an accurate measurement of density of the material while considering any porosity or structural imperfections in the sintered sample. To determine the bulk density, a formula (eqn. 4) was utilized, which takes into account the volume of material and the weight of sample in both air and when immersed in a liquid:

$$d_B = \frac{W_{dry}}{W_{dry} - W_{suspended}} \rho_{lipid} \quad (4)$$

where W_{dry} denotes the weight of dry sample; $W_{suspended}$ denotes the weight of sample when suspended in fluid. The density of fluid, typically water (ρ_{lipid}), is equivalent to 1 g/cm^3, which is the same as the density of water (ρ_{lipid} = 1 g/cm^3). A significant disparity between (d_x) and (d_B) indicates a higher level of porosity

or other structural defects within the material. CoLiFCr NPs, the X-ray density values ranged from 5.1798 g/cm^3 to 4.8072 g/cm^3, highlighting the influence of Cr substitution. The apparent porosity (P%) values were computed from the X-ray density (d_x) and bulk density (d_B) values using the following relation:

$$P = 1 - \left(\frac{d_B}{d_x}\right) \times 100$$

The porosity of CoLiFCr NPs was found to be up to 22.5%, but with the substitution of Cr, it drops and lays down to 16.5%, indicating grain expansion and fewer grain boundaries. Table-2 shows the cell volume (V), porosity (%), hopping length (L_A), (L_B), tetrahedral bond (d_{AX}), octahedral bond (d_{Bx}), tetra edge (d_{AXE}) and octa edge (d_{BXE}) shared and unshared for the CoLiFCr NPs (a = b = c).

Williamson-Hall extrapolation: The Williamson-Hall (W-H) method is a comprehensive approach to analyze peak broadening in XRD patterns, caused by both crystallite size and lattice strain. The crystallite size (t) of CoLiFCr NPs (x = 0.0-0.6) was carried out from the obtained XRD data by extrapolating the Williamson-Hall function (W-H Plot) method, to re-evaluate the Debye-Scherrer values. The linear fitted graphs were plotted against ($\beta_r \cos\theta$) and ($4\varepsilon_{str}\sin\theta$) for the preferred prominent peaks of XRD pattern (Fig. 4) and expression can be represented in eqns. 5-10 [20,21]:

Total broadening = Crystallite size broadening + Strain broadening

TABLE-2
CELL VOLUME (V), POROSITY (%), HOPPING LENGTH (L_A, L_B), TETRAHEDRAL BOND (d_{AX}), OCTAHEDRAL BOND (d_{BX}), TETRA EDGE (d_{AXE}) AND OCTA EDGE (d_{BXE}) SHARED AND UNSHARED FOR THE CoLiFCr NPs (a=b) (WHERE x = 0.0, 0.2, 0.4 AND 0.6)

x	(V) Å	P%	L_A	L_B	d_{AX}	d_{BX}	d_{AXE}	d_{BXE}	d_{BXEu}	r_A	r_B
0.0	579.67	22.50	2.516	2.437	1.891	2.035	3.088	2.805	2.948	0.571	0.713
0.2	577.59	22.47	2.514	2.435	1.889	2.033	3.085	2.802	2.945	0.569	0.711
0.4	573.02	22.34	2.514	2.434	1.889	2.032	3.084	2.802	2.945	0.569	0.711
0.6	569.92	16.50	2.507	2.428	1.882	2.025	3.074	2.792	2.935	0.562	0.704

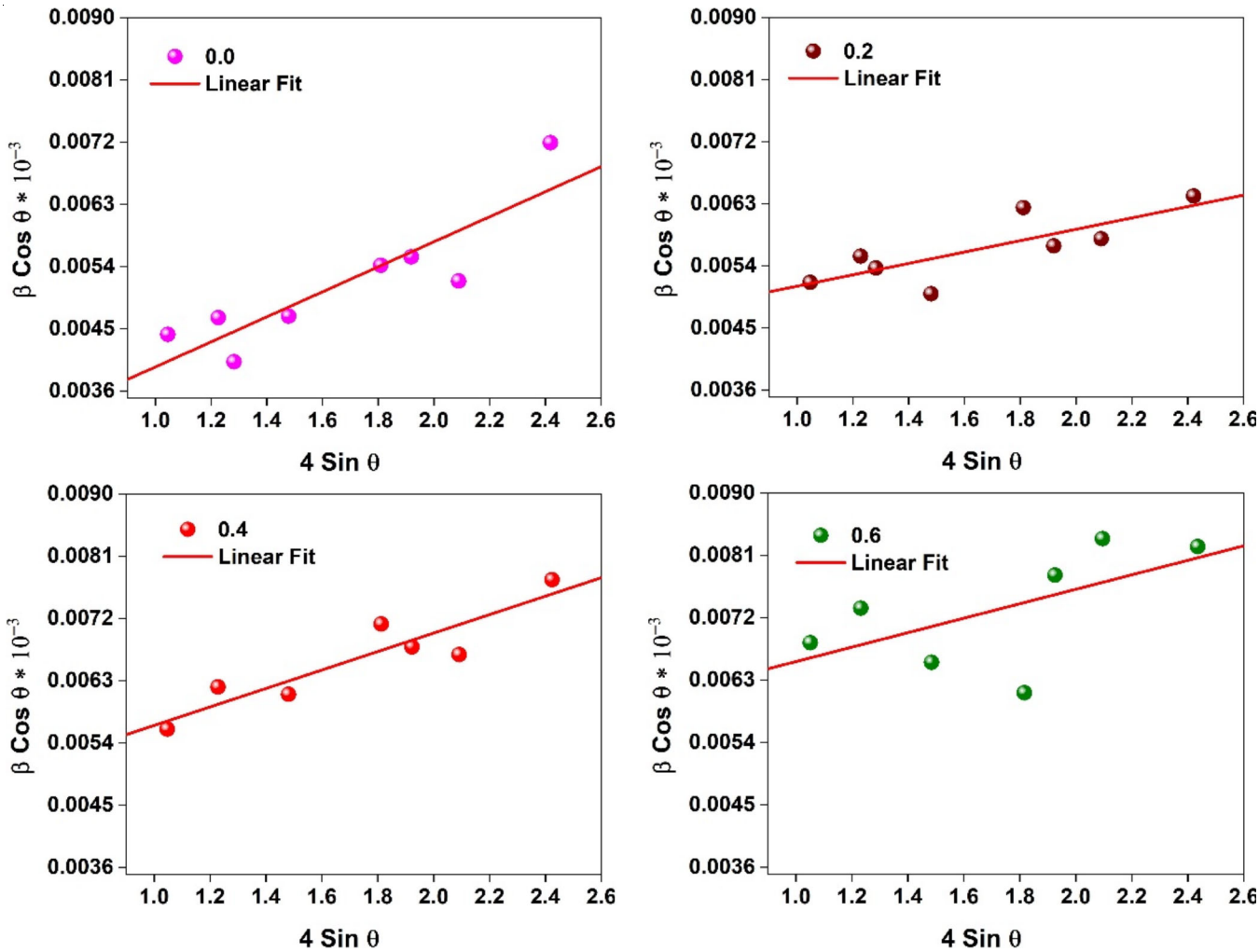

Fig. 4. Williamson-Hall plot for the CoLiFCr NPs (where x = 0.0, 0.2, 0.4 and 0.6) nanoparticles

$$\beta_{obs} = \beta_D + \beta_\delta \quad (5)$$

The observed peak broadening β_{obs} in an XRD pattern is a combination of broadening due to finite crystallite size β_D and broadening due to lattice strain β_δ.

The broadening due to crystallite size is given by Scherrer equation:

$$\beta_D = \frac{k\lambda}{D\cos\theta} \quad (6)$$

The shape factor k is generally around 0.89 for spherical particles. The variable λ represents the wavelength of X-ray, D indicates the size of crystallite and θ refers to Bragg angle.

$$\beta_T = \frac{k\lambda}{D\cos\theta} + 4\varepsilon\tan\theta \quad (7)$$

The broadening due to lattice strain is proportional to the strain ∈

$$\beta_\epsilon = 4\varepsilon\tan\theta \quad (8)$$

Substituting β_D and β_T into the total peak broadening equation, we get

$$\beta_{obs}\cos\theta = \frac{k\lambda}{D} + 4\varepsilon\sin\theta\cos\theta \quad (9)$$

$$\beta c\cos\theta = \frac{k\lambda}{D} + 4\varepsilon\sin\theta \quad (10)$$

By using the Williamson-Hall method, the crystallite size (D) and the lattice strain (∈) can be extracted from the XRD peak broadening. This approach allows for a more detailed analysis of the micro-structural properties taken from the slope and kλ/L y-intercept of the fitted line represent the particle size. While the crystallite size determined by the Williamson-Hall (W-H) plot aligns with that obtained using the Scherrer method, the variation in crystallite size is influenced by the strain correction factor included in the Williamson-Hall method, which is absent in the Scherrer method as shown in Table-3.

FTIR studies: Fig. 5 illustrates the FTIR spectrum of CoLiFCr nanoparticles (NPs) and identified the absorption frequencies ν_1 (425 cm^{-1}, 428 cm^{-1}, 428 cm^{-1}, 443 cm^{-1}) and ν_2 (535 cm^{-1}, 530 cm^{-1}, 537 cm^{-1}, 537 cm^{-1}) for functional groups in CoLiFCr NPs. At 443 cm^{-1}, the metal-oxygen (M-O) bonds are typically found in spinel structures; at 537 cm^{-1}, additional metal-oxygen interactions or lattice vibrations are represented; at 886 cm^{-1}, C-H bending vibrations from organic residues or stabilizers may be related; at 1633 cm^{-1}, C=O stretching vibrations may be from organic components in the synthesis process; and at 3292 cm^{-1}, the stretching vibrations of O-H suggest the existence of hydroxyl groups [22,23].

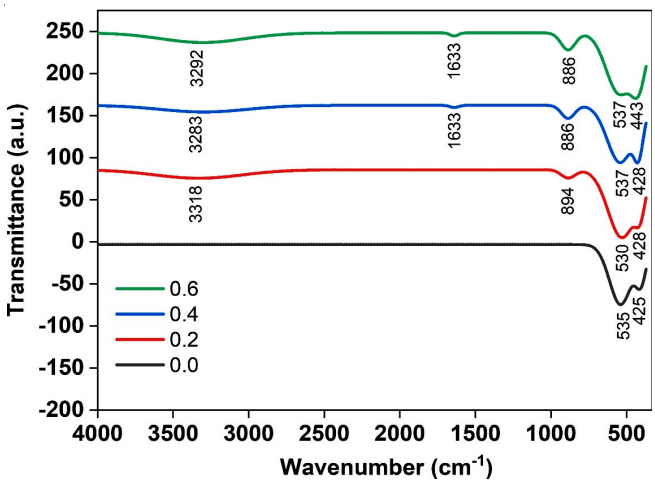

Fig. 5. FTIR spectra of CoLiFCr NPs (where x = 0.0, 0.2, 0.4 and 0.6) nanoparticles

Morphological studies

TEM studies: The qualitative analysis of CoLiFCr NPs was conducted using transmission electron microscopy (TEM) at the FEG TEM 200 kV Lab, IIT Bombay, with a Philip CM-120 instrument operating within a voltage range of 20-200 kV. It was observed that due to their magnetic properties, CoLiFCr NPs tended to aggregate into quadrate-shaped structures from the same batch. This aggregation pattern, as depicted in Fig. 6a-b showed a nano-sized distribution that aligned well with the calculations based on XRD data. The formation of pore structures within these agglomerates contributed to the relatively high surface area of nanoparticles [24]. The self-assembly behaviour of these magnetic nanoparticles (MNPs) indicated a preference for nearly spherical shapes when assembled. However, irregular nanoparticle compositions were rarely observed in TEM images of CoLiFCr NPs sample. These findings highlight the substantial influence of chromium substitution on the morphology and dimensions of cobalt lithium nanoparticles, underscoring the essential role of experimental parameters in the synthesis and characterization processes of such nanoparticles.

UV-Vis spectra: The absorbance spectra of chromium-substituted cobalt-lithium ferrite nanoparticles are illustrated in Fig. 7, highlighting their absorption properties within the ultraviolet-visible region of the electromagnetic spectrum. The UV-Vis spectroscopy reveals that various compositions (x =

TABLE-3
FWHM AND THE W-H PARAMETERS FOR THE TYPICAL CoLiFCr NPs (WHERE x = 0.0)

2θ	θ (°)	Radian (θ)	FWHM degree (θ)	FWHM radian (θ)	Cos θ	D = 0.9λ/ βCosθ	D (nm)	βcosθ	4sinθ
30.30	15.15	0.264	0.262	0.005	0.965	313.82	31.38	0.004	1.04
35.71	17.85	0.312	0.280	0.005	0.952	297.52	29.75	0.005	1.22
37.42	18.71	0.326	0.243	0.004	0.947	344.64	34.46	0.004	1.28
43.40	21.70	0.379	0.288	0.005	0.929	296.11	29.61	0.005	1.47
53.82	26.91	0.469	0.348	0.006	0.892	255.98	25.59	0.005	1.81
57.37	28.68	0.500	0.361	0.006	0.877	250.29	25.02	0.006	1.91
62.99	31.49	0.549	0.348	0.006	0.853	267.11	26.71	0.005	2.08
74.44	37.22	0.649	0.517	0.009	0.797	192.86	19.28	0.007	2.41

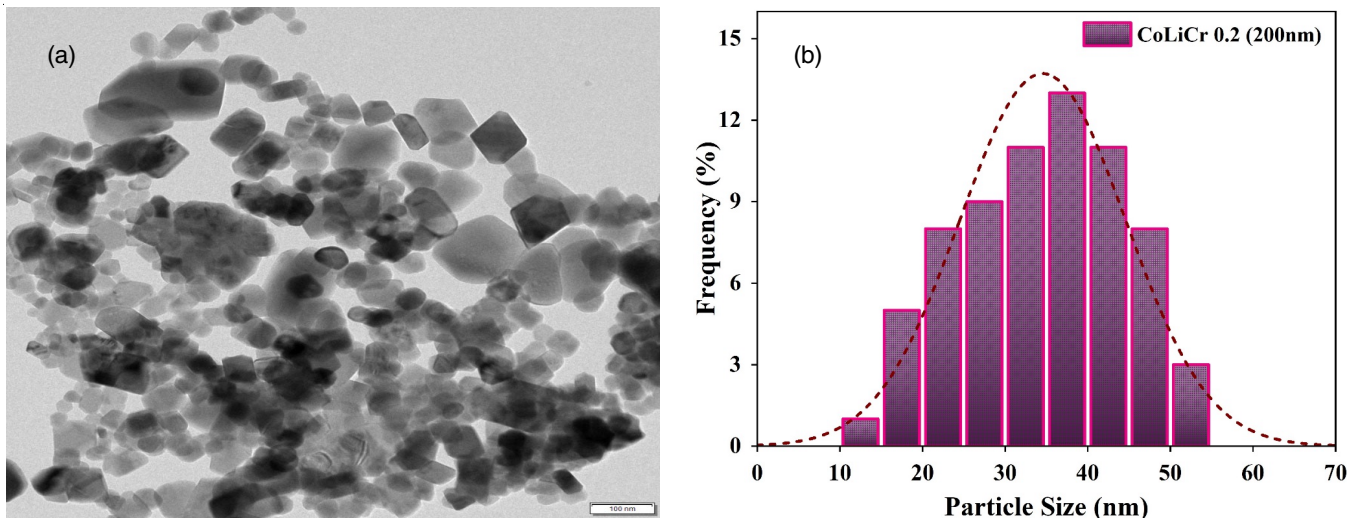

Fig. 6. HR-TEM image (a) and histogram (b) of (a) CoLiFCr NPs (x = 0.2)

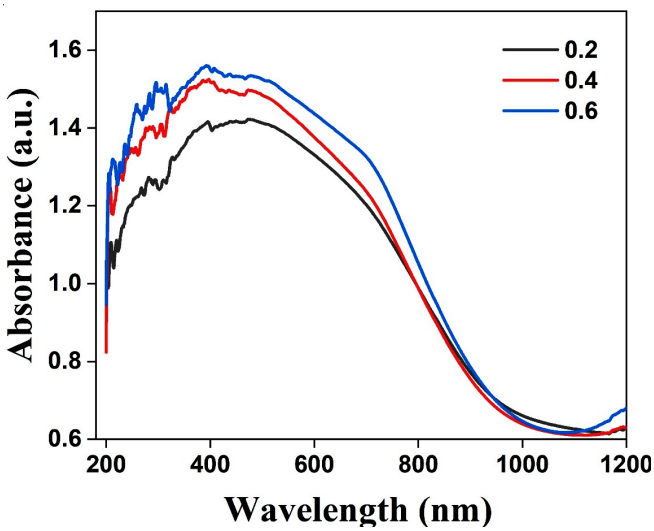

Fig. 7. UV-Vis absorbance spectra of CoLiFCr NPs (where x = 0.2, 0.4 and 0.6)

0.2, 0.4 and 0.6) display unique absorption peaks, which signify the electronic transitions occurring within the nanoparticles. The absorbance spectra exhibit significant absorption peaks spanning from approximately λ = 296 nm to λ = 477 nm for x = 0.2, λ = 289 nm to λ = 477 nm for x = 0.4 and λ = 281 nm to λ = 477 nm for x = 0.6 (Table-4). These absorption peaks correspond to transitions between energy levels within the nanoparticles, offering valuable insights into their optical properties such as band gap energy and particle size distribution [25].

TABLE-4
UV-VIS ABSORPTION AND ENERGY GAP (E_g) OF CoLiFCr NPs (WHERE x = 0.2, 0.4 AND 0.6)

x	λ (nm)	λ (nm)	λ (nm)
0.2	296	394	477
0.4	289	394	477
0.6	281	394	477

Dielectric properties: An extensive analysis was conducted on the dielectric properties of Cr-substituted Co-Li ferrite NPs within a frequency range from 50 Hz to 5 MHz, specifically focusing on compositions with x values of 0.0, 0.2 and 0.6. The study involved the measurement of dielectric constant (ε′) and dielectric loss (ε″) expressed in the relation: $\varepsilon = \varepsilon' - j\varepsilon''$; and tan δ values to assess the electrical characteristics of the nanoparticles, revealing interesting trends across different compositions and frequencies [26]. The nanoparticles with x = 0.2 displayed high ε′ values at 50 Hz, indicating strong polarization capabilities, while those with x = 0.6 exhibited a decrease possibly linked to the structural changes affecting polarization. The dielectric loss values (ε″) and tan δ values showed frequency-dependent behaviours typical of dielectric materials, with higher losses observed at lower frequencies, highlighting the energy dissipation and efficiency of the nanoparticles. Fig. 8a illustrates the inverse relationship between the dielectric constant (ε′) and frequency (50 Hz ≤ f ≤ 5 MHz), revealing its exponential nature as derived from as eqn. 11 [27]:

$$\varepsilon' = \frac{Cp \times t}{\varepsilon_0 A} \tag{11}$$

The dielectric properties of CoLiFCr NPs were examined using various parameters including capacitance (Cp), polished pellet thickness (t), cross-sectional area (A) and the permittivity of free space ($\varepsilon_0 = 8.85 \times 10^{-12}$ F/m). The dielectric loss ε″ was determined using equation $\varepsilon'' = \varepsilon' \times \tan\delta$ and it was observed that ε″ decreased exponentially with the frequency, as shown in Fig. 8b. The reductions in both ε′ and ε″ at lower frequencies can be attributed to the relaxation polarization caused by interfacial effects and electron displacement. This phenomenon is consistent with the Maxwell-Wagner interfacial polarization model, which explains the presence of Fe^{3+}, Fe^{2+} and Cr^{3+} ions at the octahedral [B]-site in the ferrite structure. The dissipation factor $D = \varepsilon''/\varepsilon'$ was used to calculate the dielectric loss tangent (tan δ) of CoLiFCr NPs and it was found that tan δ decreased with increasing frequency. Fig. 8c, demonstrates that tan δ is particularly high at lower frequencies, which could be attributed to increased resistance associated with the grain boundaries.

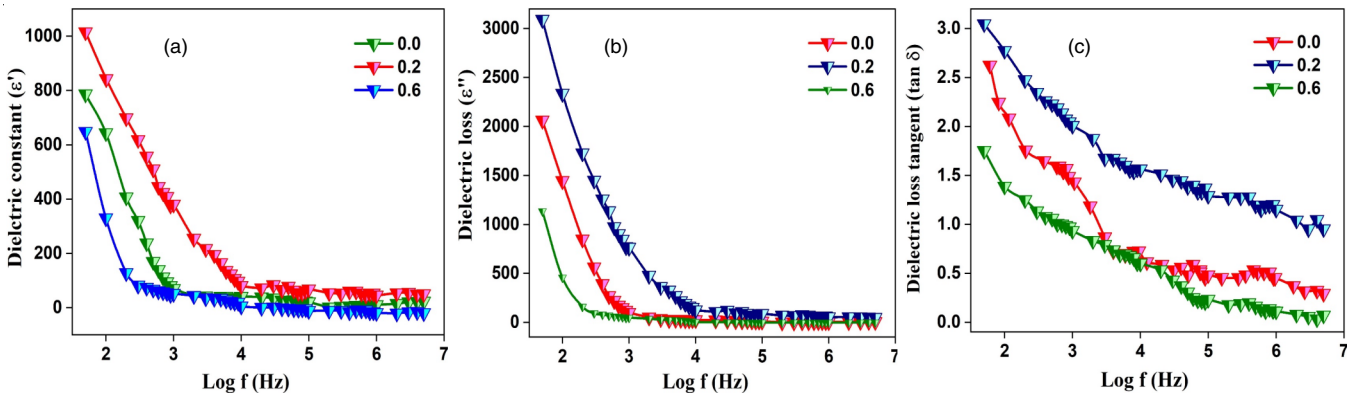

Fig. 8. Variation dielectric constant (ε′) (a), variation dielectric loss (ε″) (b) and variation dielectric loss tangent (tan δ) (c) with frequency of CoLiFCr NPs (where x = 0.0, 0.2 and 0.6)

The dielectric parameters are summarized in Table-5. Apart from polarization lag, the higher tan δ values at lower frequencies may also be influenced by factors such as doping concentration, lattice defects and material inhomogeneity [28].

DC-resistivity property: Fig. 9 illustrates the DC-resistivity and related electronic properties of Cr-substituted Co-Li ferrite NPs, (x = 0.0, 0.2, 0.4 and 0.6), were investigated to understand their electrical conductivity characteristics. These properties were evaluated using the activation energy (ΔE), charge carrier concentration (n), drift mobility (μ_d) and diffusion coefficient (D) at 860 K. The activation energy (ΔE) was determined using the Arrhenius equation [29] (eqn. 12):

$$\Delta E = \frac{-1}{k_B} \cdot \frac{\ln p}{d\left(\frac{1}{T}\right)} \quad (12)$$

where ρ is the resistivity; k_B is the Boltzmann constant and T is a absolute temperature (K). The activation energy (ΔE), which indicates the energy required for charge carriers to transition from the valence to the conduction band, ranged from 0.067 eV for x = 0.0 to 0.178 eV for x = 0.6 as depicted in Table-6. This suggests that the higher levels of chromium substitution increase the energy barrier for charge carriers. The charge carrier concentration (n) was found to decrease slightly from 0.2142 × 10^{23} cm^{-3} for x = 0.0 to 0.1638 × 10^{23} cm^{-3} for x = 0.6, indicating a trend towards fewer mobile charge carriers with increasing Cr content. Drift mobility (μ_d) and diffusion coefficient (D) measurements at 860 K showed the variations across the compositions, with values of μ_d ranging from 0.0192 × 10^{-4} cm^2 V^{-1} s^{-1} to 0.0225 × 10^{-4} cm^2 V^{-1} s^{-1} and D ranging from 1.6522 × 10^{-7} cm^2/s to 2.1962 × 10^{-7} cm^2/s. These parameters collectively contribute to understanding the electrical transport properties of Cr-substituted Co-Li ferrite nanoparticles, essential for applications in electronic devices and magnetic materials requiring controlled electrical conductivity and mobility characteristics [28].

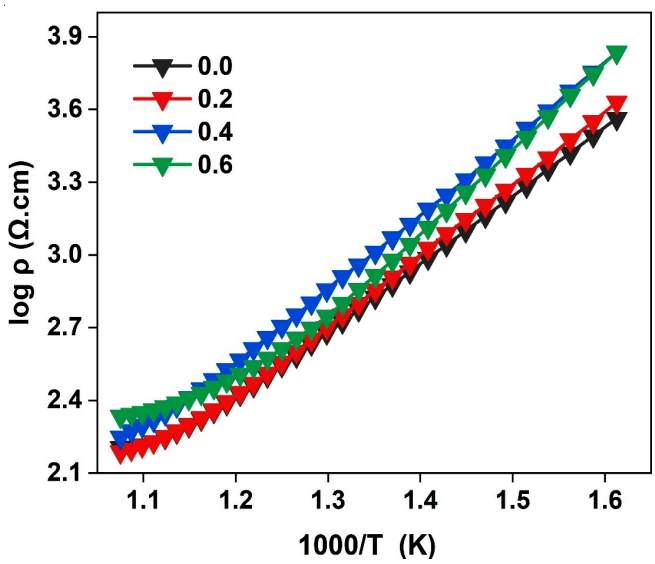

Fig. 9. DC-resistivity plots of CoLiFCr NPs (where x =0.0, 0.2, 0.4 and 0.6)

Conclusion

Cr^{3+}-substituted cobalt-lithium-based iron chromium oxide nanoparticles (CoLiFCr NPs) were effectively synthesized *via* the citric acid-assisted sol-gel auto-combustion method, utilizing a nitrate to citric acid ratio of 1:3. The X-ray diffraction analysis of CoLiFCr NPs revealed distinct Bragg reflections at the indices (220), (311), (400), (422), (511) and (440), which were matched with JCPDS card Nos. 74-2081 and 44-1485, thereby validating the establishment of a single-phase cubic spinel structure. Elemental analysis verified the stoichiometric

TABLE-5
VALUES OF DIELECTRIC CONSTANT (ε′), DIELECTRIC LOSS (ε″) AND DIELECTRIC LOSS TANGENT (tan δ) FOR CoLiFCr NPs (WHERE x = 0.0, 0.2 AND 0.6)

x	At 50 Hz			At 5 Hz		
	ε′	ε″	tan δ	ε′	ε″	tan δ
0.0	786.3362	2062.5837	2.62303	23.4205	6.8392	0.29202
0.2	1014.6090	3089.9511	3.04546	50.4154	48.0146	0.95238
0.6	648.0085	1134.5721	1.75086	-19.1635	-1.3664	0.0713

TABLE-6
ACTIVATION ENERGY, CHARGE CARRIER CONCENTRATION, DRIFT MOBILITY AND DIFFUSION COEFFICIENT OF CoLiFCr NPs (WHERE x = 0.0, 0.2, 0.4 AND 0.6)

x	ΔE activation energy (eV)	Charge carrier concentration (n) (cm^{-3})	Drift mobility (μ_d) ($cm^2\ V^{-1}\ s^{-1}$)	Diffusion coefficient (D) cm^2/s (860 K)
0.0	0.067125	0.2142×10^{23}	0.0205×10^{-4}	2.1962×10^{-7}
0.2	0.073933	0.1935×10^{23}	0.0225×10^{-4}	2.1698×10^{-7}
0.4	0.079716	0.1725×10^{23}	0.0192×10^{-4}	1.6522×10^{-7}
0.6	0.178887	0.1638×10^{23}	0.0207×10^{-4}	1.7222×10^{-7}

discharge of Fe^{3+}, Fe^{2+} and Cr^{3+} ions. The lattice constant (a) was determined to decrease from 8.338 ± 0.002 Å to 8.291 ± 0.002 Å after Cr substitution, due to the smaller ionic radii of Cr^{3+} ions compared to Fe^{3+} ions. The X-ray density values ranged from 5.1798 g/cm^3 to 4.8072 g/cm^3, reflecting the influence of Cr substitution. The crystallite size (D) was estimated from the full width at half maximum (FWHM) using the Debye-Scherrer formula, showing a decrease from approximately 29.74 nm to 18.90 nm after Cr^{3+} co-substitution, as confirmed by the Williamson-Hall (W-H) method. FTIR spectra of CoLiFCr NPs indicated the presence of metal-oxygen (M-O) bonds, characteristic of spinel structures, with key peaks at 443 and 537 cm^{-1}. TEM images revealed moderately spherical, proportionally aggregated nanoparticles, indicating a high surface area with an agglomerated distribution. The dielectric constant (ε′) was seen to be decreased with the increasing frequency (50 Hz ≤ f ≤ 5 MHz), consistent with Maxwell-Wagner interfacial polarization. The UV-Vis spectra showed absorption at λ = ~ 296 Å and ~394 Å, with no significant changes upon Cr deposition. The DC-electrical properties of CoLiFCr NPs were investigated by analyzing their DC resistivity, highlighting the impact of Cr^{3+} substitution on conductivity. This study highlights the structural, micro-structural, dielectric and magnetic properties of Cr-substituted Co-Li ferrite nanoparticles, demonstrating the potential for tuning material properties through the precise compositional modifications.

ACKNOWLEDGEMENTS

One of the authors, AAN, is grateful to Punyashlok Ahilyadevi Holkar Solapur University for allowing access to the X-ray diffraction facilities. The authors are also grateful to The Head of Chemistry Department, Dr. Babasaheb Ambedkar Marathwada University, Chhatrapati Sambhajinagar, for providing the FTIR analysis facilities.

CONFLICT OF INTEREST

The authors declare that there is no conflict of interests regarding the publication of this article.

REFERENCES

1. S. Arcaro and J. Venturini, Modern Ferrites in Engineering: Synthesis, Processing and Cutting-Edge Applications, Springer International Publishing (2021).
2. S. Dabagh, S.A. Haris and Y.N. Ertas, *ACS Biomater. Sci. Eng.*, **9**, 4138 (2023); https://doi.org/10.1021/acsbiomaterials.3c00255
3. A.A. Nawpute, S.D. Tapsale, S.S. Gawali, S.P. More and K.M. Jadhav, *J. Electron. Mater.*, **53**, 2250 (2024); https://doi.org/10.1007/s11664-024-10971-8
4. S. Panda, C.K. Biswas and S. Paul, *Ceram. Int.*, **47**, 28122 (2021); https://doi.org/10.1016/j.ceramint.2021.07.100
5. R. Yadwade, S. Kirtiwar and B. Ankamwar, *J. Nanosci. Nanotechnol.*, **21**, 5812 (2021); https://doi.org/10.1166/jnn.2021.19285
6. L. Men, S. Feng, J. Zhang, X. Luo and Y. Zhou, *Green Chem.*, **26**, 1170 (2024); https://doi.org/10.1039/D3GC04088G
7. K. Rajagopalan, B. Ramasubramanian, S. Velusamy, S. Ramakrishna, A.M. Kannan, M. Kaliyannan and S. Kulandaivel, *Mater. Circular Econ.*, **4**, 22 (2022); https://doi.org/10.1007/s42824-022-00064-4
8. N.Q. Abro, N. Memon, M.S. Kalhoro, S.H. Laghari and Z. Ali, in eds.: A.K. Bhardwaj, A.L. Srivastav, K. Dwivedi and M. Sillanpää, Fundamental Scope of Nanomaterial Synthesis from Wastes, In: Green and Sustainable Approaches using Wastes for the Production of Multifunctional Nanomaterials, Elsevier, Chap. 20, pp. 289-304 (2024).
9. A. E. Danks, S. R. Hall and Z Schnepp, *Mater. Horiz.*, **3**, 91 (2016); https://doi.org/10.1039/C5MH00260E
10. A. Mallah, F. Al-Thuwayb, M. Khitouni, A. Alsawi, J.J. Suñol, J.M. Greneche and M.M. Almoneef, *Crystals*, **13**, 894 (2023); https://doi.org/10.3390/cryst13060894
11. V. Subhiksha, M.K. Okla, P. Sivaranjani, M.A. Abdel-Maksoud, I.A. Saleh, H.A. Abu-Harirah and S.S. Khan, *Chemosphere*, **342**, 140181 (2023); https://doi.org/10.1016/j.chemosphere.2023.140181
12. S. Sarmah, D. Maji, S. Ravi and T. Bora, *J. Alloys Compd.*, **960**, 170589 (2023); https://doi.org/10.1016/j.jallcom.2023.170589
13. R. Vishwaroop and S.N. Mathad, *Sci. Sinter.*, **52**, 349 (2020); https://doi.org/10.2298/SOS2003349V
14. Z. Li, J. Dai, C. Cheng, Z. Suo and W. qing, *Mater. Res. Express*, **7**, 086102 (2020); https://doi.org/10.1088/2053-1591/abae26
15. M. Basak, M.L. Rahman, M.F. Ahmed, B. Biswas and N. Sharmin, *J. Alloys Compd.*, **895**, 162694 (2022); https://doi.org/10.1016/j.jallcom.2021.162694
16. F. De Boer, J. Van Santen and E. Verwey, *J. Chem. Phys.*, **18**, 1032 (1950); https://doi.org/10.1063/1.1747852
17. S. Jiao, R. Pang, S. Wang, H. Wu, T. Tan, S. Zhang, L. Jiang, D. Li, C. Li and H. Zhang, *Mater. Res. Bull.*, **149**, 111710 (2022); https://doi.org/10.1016/j.materresbull.2021.111710
18. M. Doumeng, L. Makhlouf, F. Berthet, O. Marsan, K. Delbé, J. Denape and F. Chabert, *Polym. Test.*, **93**, 106878 (2021); https://doi.org/10.1016/j.polymertesting.2020.106878
19. C.G. Lima, A.J. Araújo, R.M. Silva, R.A. Raimundo, J.P. Grilo, G. Constantinescu, A.V. Kovalevsky and D.A. Macedo, *J. Solid State Chem.*, **299**, 122172 (2021); https://doi.org/10.1016/j.jssc.2021.122172
20. P.S. Sundaram, T. Sangeetha, S. Rajakarthihan, R. Vijayalaksmi, A. Elangovan and G. Arivazhagan, *Physica B*, **595**, (2020); https://doi.org/10.1016/j.physb.2020.412342
21. S. Yousefi, B. Ghasemi and M.P. Nikolova, *J. Cluster Sci.*, **33**, 2197 (2022); https://doi.org/10.1007/s10876-021-02144-y

22. S.A. Saafan, M.K. El-Nimr, M.M. Hussein and M. K.Omar, *Appl. Phys., A Mater. Sci. Process.*, **127**, 1 (2021); https://doi.org/10.1007/s00339-021-04947-2
23. T. Zeeshan, S. Anjum, S. Waseem, F. Majid, M. Danish Ali and A. Aslam, *Mater. Sci. Pol.*, **39**, 139 (2021); https://doi.org/10.2478/msp-2021-0008
24. F. Ahangaran and A.H. Navarchian, *Adv. Colloid Interface Sci.*, **286**, 102298 (2020); https://doi.org/10.1016/j.cis.2020.102298
25. M.K. Singh and M.S. Mehata, *Opt. Mater.*, **109**, 110309 (2020); https://doi.org/10.1016/j.optmat.2020.110309
26. Mubasher, M. Mumtaz, M. Hassan, L. Ali, Z. Ahmad, M.A. Imtiaz, M.F. Aamir, A. Rehman and K. Nadeem, *Appl. Phys.*, *A Mater. Sci. Process.*, **126**, 334 (2020); https://doi.org/10.1007/s00339-020-03529-y
27 M. Zahid, H.M. Khan, I. Sadiq, K. Ali, M. Mirza, M.U. Islam, S.A. Buzdar and Aziz-ur-Rehman, *J. Mater. Sci.: Mater. Electr.*, **32**, 9183 (2021); https://doi.org/10.1007/s10854-021-05584-4
28. A. Raghavender and K.M. Jadhav, *Bull. Mater. Sci.*, **32**, 575 (2009); https://doi.org/10.1007/s12034-009-0087-8
29. K. Chandramouli, B. Suryanarayana, P.V.S.K. Phanidhar Varma, V. Raghavendra, K.A. Emmanuel, P. Taddesse, N. Murali, T. Wegayehu Mammo and D. Parajuli, *Results Phys.*, **24**, 104117 (2021); https://doi.org/10.1016/j.rinp.2021.104117
30. G.V. Priya, N. Murali, M. Raju, B. Krishan, D. Parajuli, P. Choppara, B.C. Sekhar, R. Verma, K.M. Batoo and P.V.L. Narayana, *Appl. Phys. A*, **128**, 663 (2022); https://doi.org/10.1007/s00339-022-05809-1